Journal of Alloys and Compounds 932 (2023) 167587

Contents lists available at ScienceDirect

Journal of Alloys and Compounds

journal homepage: www.elsevier.com/locate/jalcom

Effects of Si solution in θ-$Al_{13}Fe_4$ on phase transformation between Fe-containing intermetallic compounds in Al alloys

Zhongping Que *, Changming Fang, Chamini L. Mendis, Yun Wang, Zhongyun Fan

Brunel Centre for Advanced Solidification Technology (BCAST), Brunel University London, Uxbridge, Middlesex UB8 3PH, UK

ARTICLE INFO

Article history:
Received 17 May 2022
Received in revised form 10 October 2022
Accepted 13 October 2022
Available online 18 October 2022

Keywords:
θ-$Al_{13}Fe_4$
Silicon substitution
Phase transformation
Orientation relationship
Al alloys

ABSTRACT

θ-$Al_{13}Fe_4$ is one of the common Fe-containing intermetallic compounds (FIMCs) that forms during solidification in Al alloys. Silicon (Si) as impurity or solute in Al alloys is easily doped into θ-$Al_{13}Fe_4$, which not only causes compositional variation but also modifies the lattice parameters, and in some circumstances, modifies or changes the crystal structure of θ-$Al_{13}Fe_4$. In this study, multiple Al-Fe and Al-Fe-Si alloys which solidified θ-$Al_{13}Fe_4$ as equilibrium or non-equilibrium phase in primary or eutectic structures were designed and investigated. Different types of phase transformation among θ-$Al_{13}Fe_4$ and the other FIMCs such as α'-Al_8Fe_2Si, α-$Al_{15}(Fe,Mn)_3Si_2$ and β-Al_5FeSi were investigated with scanning electron microscopy (SEM), transmission electron microscopy (TEM) and single crystal X-ray analysis. The composition and lattice parameters of FIMCs observed in this study were measured by TEM and X-ray analysis. The orientation relationships between θ-$Al_{13}Fe_4$ and the other types of FIMCs (α'-Al_8Fe_2Si, α-$Al_{15}(Fe,Mn)_3Si_2$ and β-Al_5FeSi) were determined with TEM analysis. The phase selection and solidification sequence were investigated by comparing the phase diagram calculation and the casting experiments. The configuration entropy of FIMCs was calculated to build up structural models. Finally, the influence of incorporation of Si into θ-$Al_{13}Fe_4$ on the phase transformation between θ-$Al_{13}Fe_4$ and the other types of FIMCs were discussed from crystallographic and thermal stability perspectives.

1. Introduction

Iron (Fe) is inevitably picked up during the fabrication of primary Al, and it cannot be removed completely during recycling [1,2]. Due to the low solid solubility in aluminum especially at the low temperature, the Fe usually forms intermetallic phases in Al alloys, such as θ-$Al_{13}Fe_4$, α-$Al_{15}(Fe, Mn)_3Si_2$, and β-Al_5FeSi, etc. [4–7]. These Fe-containing intermetallic compounds (FIMCs) usually form as large particles with different morphologies, such as plate-like, needle-like, Chinese script [7–11]. They deteriorate the mechanical properties dramatically, especially the ductility. In the last decades, much effort has been made to reduce the detrimental effect on the mechanical properties, such as removal of Fe, modification of FIMCs morphology, and refinement of FIMCs, etc. However, it is reported that [12] the removal Fe is very limited when Fe is lower than 0.7 wt%, which is still undesirable for the mechanical properties. The techniques or theories on direct removal of iron from aluminum has so far made no satisfactory progress. Some transition metal elements such as Mn, Co, and Cr were used to modify the morphology of FIMCs [13–17]. However, these elements will increase the total amount of FIMCs, which is also harmful to the mechanical properties of Al alloys. In recent years, research has focused to some extent on the development of grain refinement techniques for these FIMCs by applying the heterogeneous nucleation theory [10,18–20]. The bottlenecks in technology development are due to the lack of the fundamental understanding on the formation mechanism of FIMCs and the relationship between different types of FIMCs. In recent years, our group has worked on the understanding on the heterogeneous nucleation of FIMCs and phase relationship between different types of FIMCs by investigating different types of phase transformation among these FIMCs experimentally and using crystallographic methods [21–24].

Many different types of FIMCs were reported in various Al-alloys. In Al-Fe-Si casting alloys, the most commonly observed FIMCs are θ-$Al_{13}M_4$ (M= Fe, Ni, Cr, Cu, etc.) (monoclinic), β-Al_5FeSi (monoclinic), α-$Al_{15}(Fe, Mn)_3Si_2$ (complex body-centered cubic (BCC)) and α'-Al_8Fe_2Si (complex hexagonal) [3–6,25]. The formation of these FIMCs is very sensitive to the alloy composition. The composition and lattice parameters of these FIMCs change with the alloy composition and formation conditions. These FIMCs have a range of compositions and lattice parameters, and they act like the "solid solution compounds". For example, atomic positions of Al in θ-$Al_{13}Fe_4$, α-Al_{15}(Fe,

* Corresponding author.
E-mail address: Zhongping.Que@brunel.ac.uk (Z. Que).

https://doi.org/10.1016/j.jallcom.2022.167587

$Mn)_3Si_2$ can be replaced with Si, and the atomic positions of Fe are substituted by other transition elements such as Mn or Cr. This also the case for the other FIMCs such as β-Al_5FeSi and α'-Al_8Fe_2Si. The alloying elements incorporated into the parent FIMCs not only causes change in crystal structure but also induce phase transition, e.g., Mn doping in β-Al_5FeSi (monoclinic) cause transformation into α-$Al_{15}(Fe, Mn)_3Si_2$ (BCC). The modification achieves more desirable types of FIMCs in terms of retaining mechanical properties especially the ductility by modifying the morphology of the FIMCs. However, the modification result in complicated heterogeneous nucleation and phase transformation process among different types of FIMCs, which makes the microstructure control even more difficult.

θ-$Al_{13}Fe_4$ as one of the most common FIMCs in as-cast Al alloys is reported a monoclinic crystal structure with lattice parameters: a = 15.447 Å, b = 8.057 Å, c = 12.429 Å and β = 107.80° [6]. It has a monoclinic lattice with space group C2/m (nr. 12) [13]. There are 20 crystallographically different atomic sites (5 Fe and 15 Al) and 102 atoms in total in a unit cell. The Al atoms have 10–12 neighbours including 2–4 Fe, except the Al2 atoms at the Wyckoff 4i sites which have only 6 neighbours including two Fe with Fe-Al bond-lengths below 3.0 Å (1 Å = 0.1 nm = 10^{-10} m). θ-$Al_{13}Fe_4$ is an extremely impurity tolerant intermetallic compound as both Al and Fe may be substituted with other elements, such as Si, Cr, Ni, Mn, etc. [26–31]. Experiments show that Si can easily incorporate into the θ-$Al_{13}Fe_4$ at impurity or solute concentration levels in Al alloys. The elemental solution and the composition changes in FIMCs not only can cause the lattice parameters variation, but also can lead to phase transformation [21,22,32–34]. Research published recently [21] reported the multi-step phase transformation from θ-$Al_{13}Fe_4$ to the other types of FIMCs α'-Al_8Fe_2Si, β-Al_5FeSi and δ-Al_4FeSi_2. The variation on the phase transformation among the FIMCs have been reported in literature to be dependent on the composition and cooling conditions. The experimental evidence shows that the multi-step phase transformation from θ-$Al_{13}Fe_4$ to the other types of FIMCs is a diffusion-controlled phase transformation which is mainly affected by the Si diffusion.

However, the understanding of the reasons behind the variable phase transformation among the FIMCs is very limited due to the lack of the fundamental research on the mechanisms of phase transformation, the phase relationships, and the changes in crystal structure during the experiment. Our research group focus on the fundamental research on formation and grain refinement of FIMCs in Al alloys recent years. In this paper, we summarized the findings on the phase transformation between θ-$Al_{13}Fe_4$ and the other types of FIMCs in a number of Al alloys with different Si, Fe ratios. The effect of Si dissolution on the crystallography and the internal defects of the θ-$Al_{13}Fe_4$ crystals in different Al alloys were investigated. The phase relationship between θ-$Al_{13}Fe_4$ and the other FIMCs were investigated using TEM and single crystal X-ray analysis. The Si solubility in multiple types of FIMCs were investigated through the development of the structural models of different types of FIMCs. Finally, a mechanism of phase transformation between θ-$Al_{13}Fe_4$ and the other FIMCs is proposed.

2. Experimental

In this study, numbers of Al casting alloys containing θ-$Al_{13}Fe_4$ which phase transformed into other types of FIMCs were investigated. The phase diagrams of these Al alloys were calculated using Pandat software using PanAluminum 2020 database [48]. The alloy compositions of these Al alloys were listed in Table 1. The starting materials (in wt%) used in this work were high purity (HP) Al (99.99%), commercial purity (CP) Al (> 99.86%), Al-45Fe, Al-20Mn, Al-50Si and CP Mg (> 99.8%) master alloys. The melting temperatures of these alloys were calculated with the Pandat software using Scheil solidification model, as shown in Table 1. The casting temperatures are about 50 °C above the melting temperatures of these alloys. The alloys were produced by melting HP Al or CP Al and the master alloys in an electric resistance furnace. The master alloys were added to the molten HP Al or CP Al melts in the sequence of Al-Fe, Al-Mn, Al-Si (as required for the alloy), following by a completely mixing and sufficiently long holding time to ensure chemical homogeneity of the melt. The preheated CP Mg (200 ℃) covered with Al foil (as required by some alloys) was inserted into the melt as the last addition. After sufficiently mixing and holding isothermally for 20 min, the slag in these Al alloys was removed and cast into TP-1 moulds preheated to 380 ℃ [35]. To achieve the samples with bigger particles for single crystal X-ray tests, the remainder of melt in the crucibles was cooled to 200 ℃ in the furnace, with an average cooling rate of 0.01 K/s.

In addition to experimental alloys, an Al-3.7Ti-1B master alloy which contains 1 wt% Si and 1.5 wt% Fe was also investigated. This alloy was produced by adding Al-Fe and Al-Si master alloys into the Al-3.7Ti-1.5B master alloy melt, and casted at 1 K/s in a steel mold into a flat sample with thickness of 1–5 mm was achieved. The casting procedure in details will be reported in our other contributions [36]. In this alloy, TiB_2 particles formed in Al-Fe-Si alloy with 0.4 wt% free Ti. Therefore, to simplify, we refer this alloy containing Al-1.5Fe-1Si-3.7Ti-1B as Al-1Si-1Fe alloy. In this study, the focus is on the phase transformation between FIMCs. An AlFe intermetallic compound with B2-type (CsCl) was observed. The phase transformation between AlFe and θ-$Al_{13}Fe_4$ was examined with the aid of this alloy. A square sample was sectioned from the flat sample of Al-1Si-1Fe alloy. The microstructural characterization was carried out on the middle of the thickness by grounding and polishing both surface of the flat sample. Samples for microstructural characterisation were prepared from the cross section of TP1 samples at the 38 mm height from the bottom which solidifies at 3.5 K/s [35], with the exception of Al-1Si-1Fe alloy. Metallographic specimens were prepared using the standard procedures. To observe the 3-dimensional morphology of the structure, the samples were gently etched in 10 vol% HCl+H_2O solution for a few minutes followed by cleaning in ethanol. The as-solidified microstructure characteristics of the samples were examined using a Zeiss optical microscope fitted with the Axio Vision 4.3 image analysis system and a Zeiss Supra 35, field emission gun scanning electron microscope (FEG-SEM), operated at an accelerating voltage between 5 and 20 kV. Thin foils for high resolution transmission electron microscopy (TEM) examinations were prepared from samples which were mechanically ground and cut into 3 mm diameter discs. The discs were then manually ground to a thickness of less than 50 µm, followed by ion-beam-thinning using a Gatan precision ion polishing system (PIPS) at an energy of 2.0–5.0 kV and an incident angle of 3–5°. TEM examination was performed on a JEOL 2100 F transmission electron microscope equipped with EDX spectrometer operated at an accelerating voltage of 200 kV. The 3-dimensional morphology of the FIMCs was examined on Zeiss X radial 410 Versa X-ray –microscope operating at 80 kV with power set to 10 W to achieve the clearest image of intermetallic particles.

To investigate the crystal structure variation of FIMCs, the FIMCs crystal from different samples were examined with a single crystal X-ray diffraction. The lattice parameters from the literature and the casting conditions of samples examined are shown in Table 3. The slowly cooled samples were deep etched in 5–10% HCl+H_2O solution for a few minutes followed by ultrasonic cleaning in ethanol. After deep cleaning and drying, the large crystals of intermetallic particles from desired microstructure was cut under optical microscope and transferred to a clean glass slide. The crystal samples were further cut into the desired size (< 100 µm) for the single crystal analysis. Single crystal data were collected at 100 K using a Rigaku SuperNova, Dualflex, AtlasS2 diffractometer with Cu-Kα radiation (λ = 1.54184 Å). CrysAlis Pro software was used for data collection, absorption correction and data reduction.

Table 1
Alloy compositions (wt%) studied in this paper.

Alloys	Calculated melting temperature with Scheil model (℃)	Calculated equilibrium phase with Scheil model	Pouring temperature (℃)	Al	Fe	Mn	Si	Mg
Al-3Fe (HP Al)	805	θ-$Al_{13}Fe_4$	860	balance	3.25	0.01	–	–
Al-1Fe (CP Al)	666	θ-$Al_{13}Fe_4$	720	balance	1.02	0.01	0.03	0.004
Al-1Fe-1Si-3.7Ti-1.5B				balance	1.52	0.01	0.99	0.10
Al-4Fe-4Si	715	θ-$Al_{13}Fe_4$	760	balance	4.10	0.05	4.21	0.003
Al-5Mg-2Si-0.7Mn-1.2Fe	662	α-Al_{15}(Fe, Mn)$_3Si_2$	720	balance	1.29	0.68	2.11	5.43

In order to get reliable information about the effects of Si solution on the stability and structural information about the related FIMCs, we performed first-principles study on these compounds [24,41]. We utilized a plane-wave approach which is implanted into the first-principles code VASP (Vienna Ab initio Simulation Package) [46]. The Generalized Gradient Approximation (GGA-PBE) [47] was used for the exchange and correlation energy terms. We used a cut-off energy of 550 eV for the wave functions and the cut-off energy of 700 eV for the augmentation functions. More details are included in [24,41].

3. Results

3.1. θ-$Al_{13}Fe_4$ in Al-Fe alloys

Si as one of the major impurities in Al alloys is easily picked up during casting or from the master alloys. It is reported that Si can dope in θ-$Al_{13}Fe_4$ by replacing the Al atoms. The effects of the Si on the crystal structure and the consequently phase transformation of θ-$Al_{13}Fe_4$ will be investigated in this study. Firstly, the initial structure of the θ-$Al_{13}Fe_4$ free of Si was investigated as the reference. To produce such high pure θ-$Al_{13}Fe_4$ particles, the high pure Al and the Al-45Fe master alloy were used to minimize the effect of Si impurity. The high pure Al was previously melted at 900 ℃, and then the Al-45Fe master alloy was added into the Al melt with completely stirring until fully molten. An Al-3Fe alloy actually containing 3.25 ± 0.5 wt% Fe was produced.

To compare the effect of Si as impurity on the θ-$Al_{13}Fe_4$ phase, the other Al-1Fe alloy was produced with commercial pure Al and same Al-45Fe master alloy. The commercial pure Al was previously melted at 750 ℃, and then the Al-45Fe was added into the Al melt and stirred until fully molten. The final composition of these two alloys were list in Table 1. It shows that the Si content in Al-3Fe is negligible when HP Al was used. The measured EDX composition of θ-$Al_{13}Fe_4$ phase (Table 2) show that the Si concentration in (HP) Al-3Fe is negligible, but 0.3at% Si can be detected in the (CP) Al-1Fe. The single crystal X-ray results are shown in Table 3. The lattice parameters *a*, *b*, and *c* in θ-$Al_{13}Fe_4$ in (HP) Al-3Fe are larger than that of θ-$Al_{13}Fe_4$ in (CP) Al-1Fe. Table 3 also indicates that the lattice parameters *a*, *b*, and *c* of θ-$Al_{13}Fe_4$ decreased with the increase in Si concentration.

The as-cast microstructure of the (HP)Al-3Fe, Fig. 1, shows the typical star-like primary θ-$Al_{13}Fe_4$ phase and the needle-like θ-$Al_{13}Fe_4$ + α-Al eutectic structure (Fig. 1a). The 3D morphology of these two structures were shown in Fig. 1b-c, respectively. Fig. 1b shows that the primary θ-$Al_{13}Fe_4$ phase has the multi-faceted star-like morphology in cross section. The eutectic θ-$Al_{13}Fe_4$ phase associated with the primary θ has plate-like morphology, as shown in Fig. 1b. Some eutectic θ-$Al_{13}Fe_4$ phase was observed as needle-like morphology which is away from primary θ, as illustrated in Fig. 1c. There is no appreciable difference in the morphology of θ-$Al_{13}Fe_4$ in HP Al-3Fe and CP Al-3Fe (Fig. 1d) except the particle size.

Fig. 2a shows the bright field TEM image presenting the needle-like morphology of eutectic θ-$Al_{13}Fe_4$ phase in (CP)Al-1Fe alloy solidified from 720 ℃ at a cooling rate of 3.5 K/s. Two different types of faceted planes were observed on θ-$Al_{13}Fe_4$ phase, Fig. 2b-c. The high resolution TEM (HRTEM) images show the faceted (010) planes and (102) planes of θ-$Al_{13}Fe_4$ phase when viewed along the [$\bar{2}$01] zone direction.

As reported [37], θ-$Al_{13}Fe_4$ can be twinned easily. In as-cast Al-1Fe (CP Al) alloy, the twinning structure of θ-$Al_{13}Fe_4$ is readily observed. One example is shown in Fig. 3. The HRTEM image (Fig. 3a) and the corresponding selected area diffraction (SAED) patterns (Fig. 3b-c) show that the θ-$Al_{13}Fe_4$ crystal has leaf-like symmetrical twinning. The SAED pattern, Fig. 3d, contains two overlapping patterns with a 36 ± 0.5° rotation angle between the two sets of the SAED patterns. This provides for tenfold twins, as the orientation difference between neighbouring twins are very close to 36°. The higher magnification HRTEM image, Fig. 3e, shows that in the very localised areas, there are multi-step twinning and some disordered regions.

3.2. θ-$Al_{13}Fe_4$ in Al-4Fe-4Si alloy

Section 3.1 reported the result that Si can incorporate in θ-$Al_{13}Fe_4$ at impurity concentration level in Al alloys. Here, the effect of Si on the crystal structure of θ-$Al_{13}Fe_4$ in Al-Si-Fe alloys will be investigated. An Al-4Si-4Fe alloy with approximately equal concentration of Si and Fe (wt%) was designed and cast. The Al alloy in this work had a composition of 4.21 ± 0.5 Si, and 4.10 ± 0.6 Fe (in wt %) with Al balance. The phase diagram of the Al-4Fe-*x*Si system was calculated with the Pandat software and its associated Al-database

Table 2
TEM-EDXs composition of FIMCs phases.

Alloys	FIMCs	Composition (at%)				Technique
		Al	Fe	Mn	Si	
Al-3Fe (HP Al)	θ-$Al_{13}Fe_4$	83.5 ± 0.4	16.5 ± 0.1	–	–	SEM
Al-1Fe (CP Al)	θ-$Al_{13}Fe_4$	80.8 ± 0.4	18.9 ± 0.1	0.0	0.3 ± 0.0	TEM
Al-1Fe-1Si	θ-$Al_{13}Fe_4$	78.9 ± 0.4	18.8 ± 0.1	–	2.4 ± 0.1	TEM
Al-1Fe-1Si	AlFe	79.1 ± 0.4	19.3 ± 0.1	–	1.5 ± 0.1	TEM
Al-4Fe-4Si	θ-$Al_{13}Fe_4$ (P)	76.3 ± 0.6	20.6 ± 0.5	0.4 ± 0.05	2.7 ± 0.2	TEM
Al-4Fe-4Si	α'-Al_8Fe_2Si	74.4 ± 0.3	15.3 ± 0.1	–	10.4 ± 0.1	TEM
Al-4Fe-4Si	β-Al_5FeSi	69.2 ± 0.3	13.8 ± 0.1	–	16.9 ± 0.1	TEM
Al-5Mg-2Si-0.7Mn-1.3Fe	θ-$Al_{13}Fe_4$	74.0 ± 0.4	17.7 ± 0.2	6.4 ± 0.1	1.8 ± 0.1	SEM
Al-5Mg-2Si-0.7Mn-1.3Fe	α-Al_{15}(Fe, Mn)$_3Si_2$	75.9 ± 0.5	11.2 ± 0.2	7.4 ± 0.1	5.5 ± 0.1	SEM

Table 3
Measured crystal lattice parameter of FIMCs phases.

Alloys	FIMCs	Lattice parameters						Technique
		a(Å)	*b*(Å)	*c*(Å)	α(º)	β(º)	γ(º)	
Al-3Fe (HP Al) (0.01 K/s)	θ-$Al_{13}Fe_4$ (0at%Si)	15.4824(3)	8.08146(15)	12.4689(3)	90	107.689(2)	90	Single crystal
Al-1Fe (CP Al) (0.01 K/s)	θ-$Al_{13}Fe_4$ (0.3at%Si)	15.447(4)	8.0567(10)	12.429(2)	90	107.83(2)	90	Single crystal
Al-4Fe-4Si (0.01 K/s)	θ- $Al_{13}Fe_4$ (2.4at% Si)	15.4239(11)	8.0521(5)	12.4040(8)	90	107.649(7)	90	Single crystal
Al-1Si-1Fe-(3.7Ti-1.5B) (1 K/s)	Al Fe	2.91	–	–	–	–	–	TEM
Al-5Mg-2Si-0.7Mn-1.3Fe(0.01 K/s)	α-Al_{15}(Fe, Mn)$_3Si_2$(P)	12.61846(12)	12.61846(12)	12.61846(12)	90	90	90	
Al-4Si-4Fe (3.5 K/s)	α'-Al_8Fe_2Si	12.13	12.13	26.68	90	90	120	TEM
Al-4Si-4Fe (3.5 K/s)	β-Al_5FeSi	6.16	6.18	20.97	90	–	90	TEM
Al-5Mg-2Si-0.7Mn-1.2Fe (3.5 K/s)	θ-$Al_{13}Fe_4$	15.864	–	12.571	–	–	–	TEM
Al-5Mg-2Si-0.7Mn-1.2Fe (3.5 K/s)	α-Al_{15}(Fe, Mn)$_3Si_2$	12.70	12.70	12.70	90	90	90	TEM
–	θ-$Al_{13}Fe_4$	15.489	8.083	12.476	90	90	107.72	[6]
–	α'-Al_8Fe_2Si	12.404	12.404	26.234	90	90	120	[7]
–	β-Al_5FeSi	6.1676	6.1661	20.8093	90	91	90	[4]
–	α-Al_{15}(Fe, Mn)$_3Si_2$	12.56	12.56	12.56	90	90	90	[3]

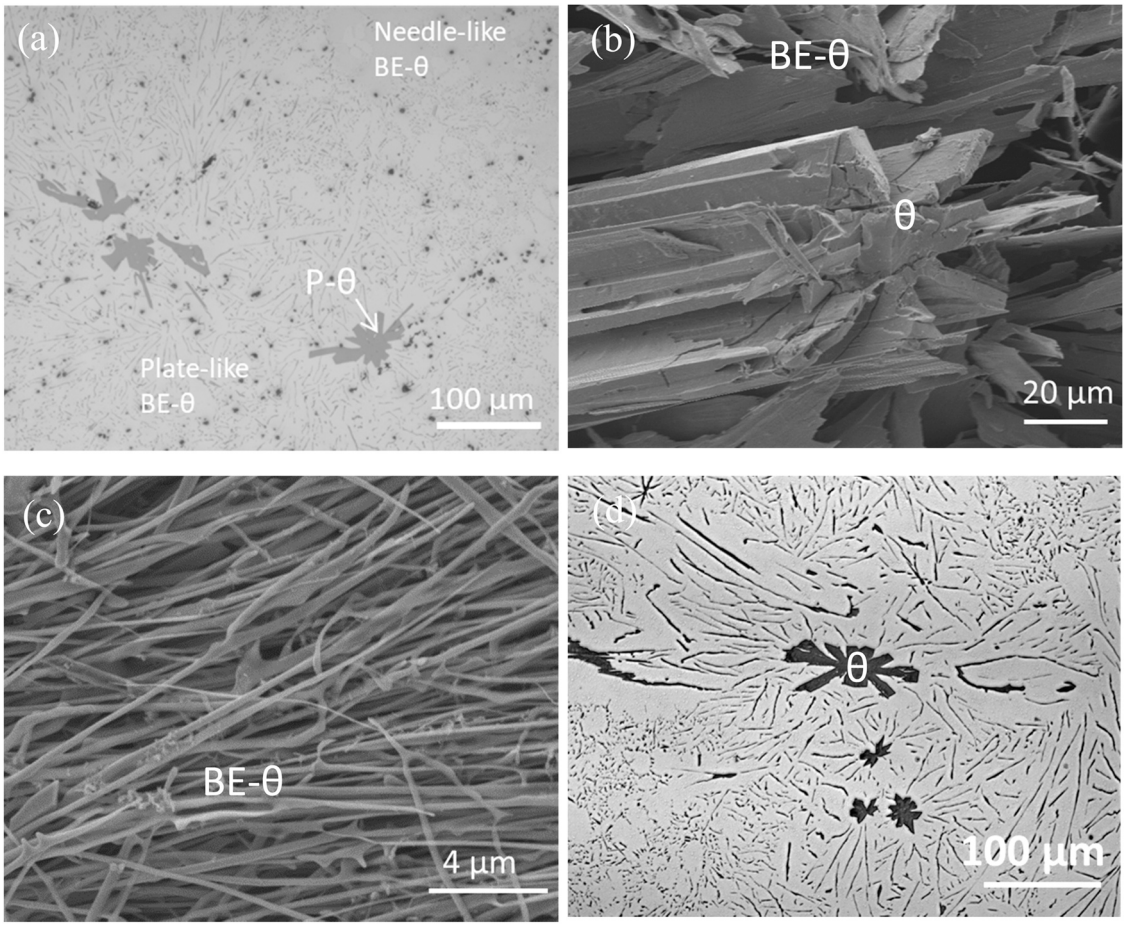

Fig. 1. (a) The optical microstructure of Al-3Fe showing the primary θ-$Al_{13}Fe_4$ and the (θ-$Al_{13}Fe_4$ + α-Al) eutectic in Al-3Fe alloy (HP Al), (b) and (c) SEM images showing the 3-dimensional morphology of (b) star-like primary θ-$Al_{13}Fe_4$ and (c) needle or plate-like eutectic θ-$Al_{13}Fe_4$ (E-θ), and (d) the optical microstructure of primary θ-$Al_{13}Fe_4$ and the (θ-$Al_{13}Fe_4$ + α-Al) eutectic in Al-3Fe alloy (CP Al).

as shown in Fig. 12b. It shows that the θ-$Al_{13}Fe_4$ is calculated as the primary equilibrium phase. The melting temperature of Al-4Fe-4Si is calculated as 715 ℃ with the Scheil solidification model. The microstructure of Al-4Si-4Fe alloy cast from 770 ℃ at a cooling rate of 3.5 K/s is shown in Fig. 4. The microstructure consisted of multiple types of FIMCs which have star-like (θ-$Al_{13}Fe_4$) and compacted morphology (α'-Al_8Fe_2Si), and multiple FIMCs in eutectic structures which have Chinese script morphology (α'-Al_8Fe_2Si) and needle-like morphology (θ-$Al_{13}Fe_4$). All the phases in this study were identified with SEM-EDX and subsequent TEM analysis. The details of primary star-like θ-$Al_{13}Fe_4$ was examined carefully with SEM, and the results are shown in Figs. 4b-c. Fig. 4b shows the high magnification SEM-BSE (backscattered electron) image of a primary θ-$Al_{13}Fe_4$ particle with a brighter central phase (θ-$Al_{13}Fe_4$) and grey surface phase (α'-Al_8Fe_2Si). The interface between θ-$Al_{13}Fe_4$ and α'-Al_8Fe_2Si presents irregular under SEM-BSE observation. The morphology in Fig. 4b indicates a reaction typical of a transformation: L + θ-$Al_{13}Fe_4$ → α'-Al_8Fe_2Si+ α-Al.

It is noted that more than one type of phase transformation was observed on the surface of primary θ-$Al_{13}Fe_4$. Fig. 4c shows the primary θ-$Al_{13}Fe_4$ particle with bright white central region (θ-$Al_{13}Fe_4$) and sharp needle-like grey surface phase (β-Al_5FeSi). The

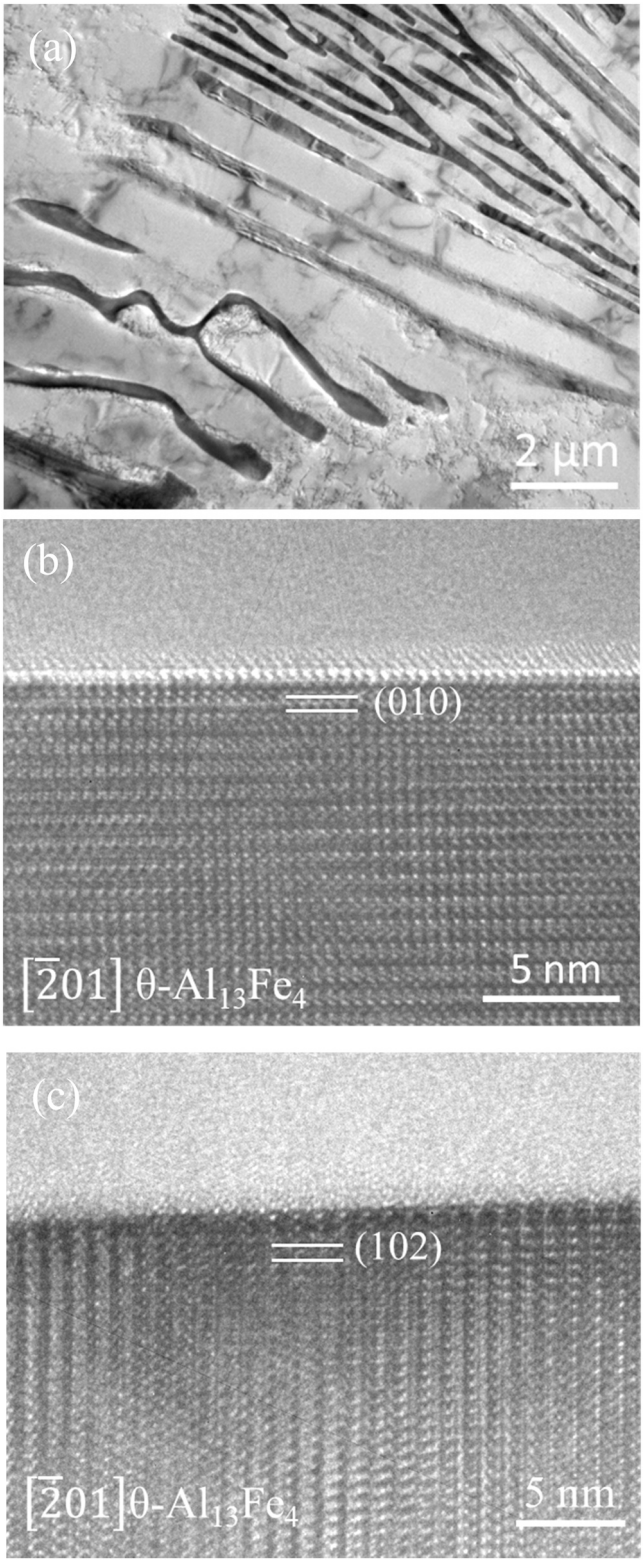

Fig. 2. (a) Bright field TEM image showing the needle-like morphology of eutectic θ-$Al_{13}Fe_4$ phase in (CP)Al-1Fe alloy, and high resolution TEM (HRTEM) images show two different faceted planes (b) (0 1 0) planes and (c) (1 0 2) planes of θ-$Al_{13}Fe_4$ phase in Al-1.0Fe binary alloy cast from 720 °C at a cooling rate of 3.5 K/s.

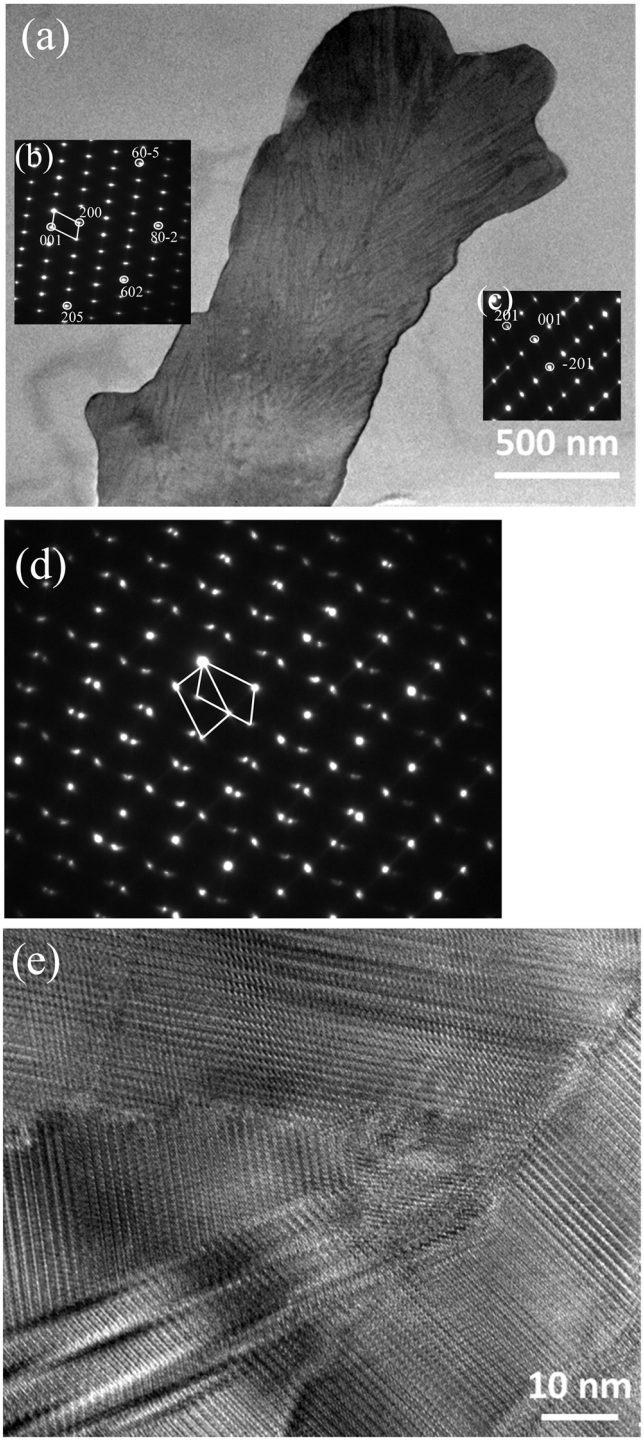

Fig. 3. (a) The low magnification bright field TEM image showing a leaf-like θ-$Al_{13}Fe_4$ crystal in (CP Al)Al-1Fe alloys with inserted selected area diffraction patterns (SAED) (b) for left half part and (c) for right half part when viewed along the [0 1 0] zone direction of θ-$Al_{13}Fe_4$, and (d) the SAED pattern indicating the relationship between two regions with a twin interface, showing a 36 ± 0.5° angle between two neighbours, (e) HRTEM image showing the twinning features in details from (a).

interface is irregular based on SEM observations. The morphology in Fig. 4c also indicates a reaction: L + θ-$Al_{13}Fe_4$ → β-Al_5FeSi+ α-Al.

The TEM-EDX compositions of θ-$Al_{13}Fe_4$, α'-Al_8Fe_2Si and β-Al_5FeSi observed in this alloy are listed in Table 2. The θ-$Al_{13}Fe_4$ phase contains 2.7 ± 0.2at%Si. However, the transformed α'-Al_8Fe_2Si and β-Al_5FeSi have much higher Si concentration at 10.4 ± 0.1at% and 16.9 ± 0.1at%, respectively.

To investigate the phase transformation mechanisms between θ-$Al_{13}Fe_4$ and the other FIMCs, the interface between θ-$Al_{13}Fe_4$/FIMCs were observed under TEM. The orientation relationships between the parent θ phase and the transformed FIMCs are examined from

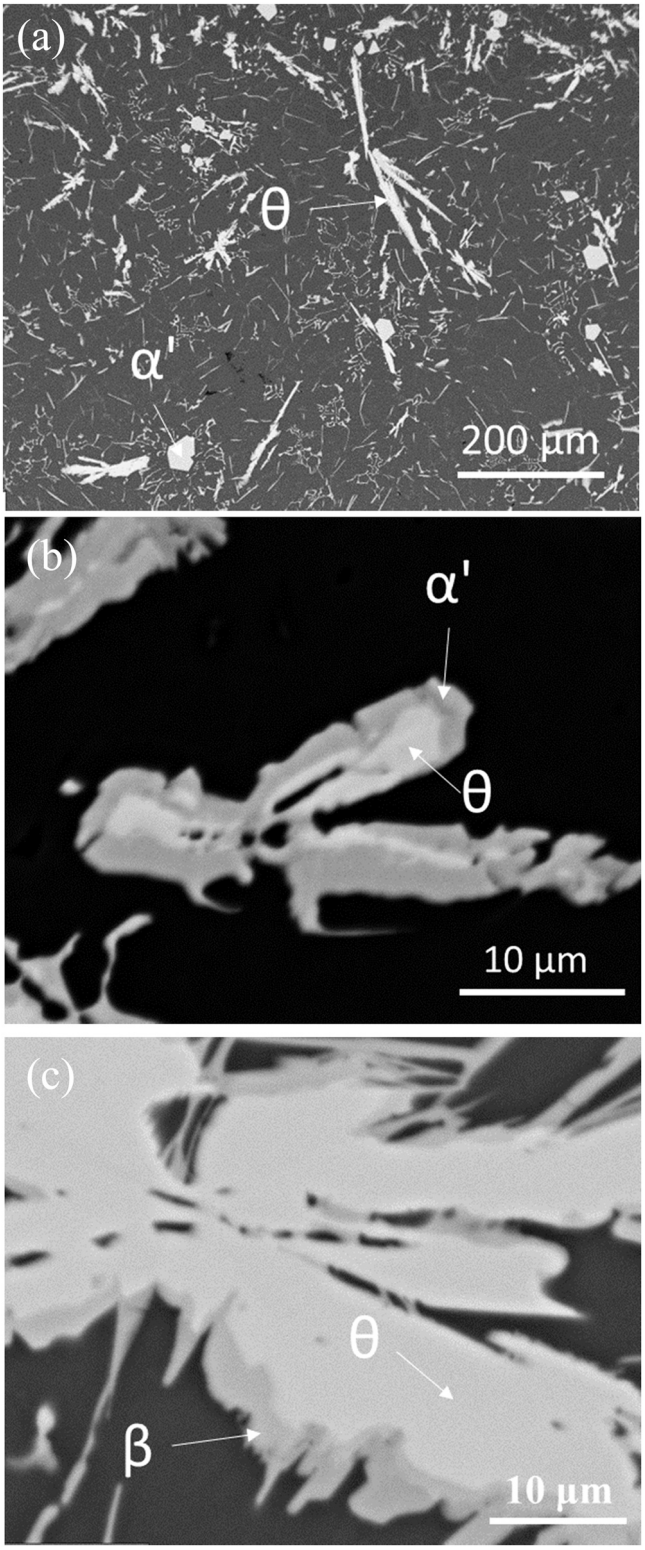

Fig. 4. SEM-BSE images showing the microstructure of (a) Al-4Si-4Fe ternary alloy which solidified at 3.5 K/s, indicating a microstructure with star-like primary θ-$Al_{13}Fe_4$, some compacted primary α'-Al_8Fe_2Si, and eutectic structures, and high magnification of SEM image of (a) indicating that (b) the primary θ-$Al_{13}Fe_4$ phase had transformed into the other FIMCs from the edge to centre with a compacted morphology, and the θ-$Al_{13}Fe_4$ phase transformed into the other FIMCs with plate-like morphology.

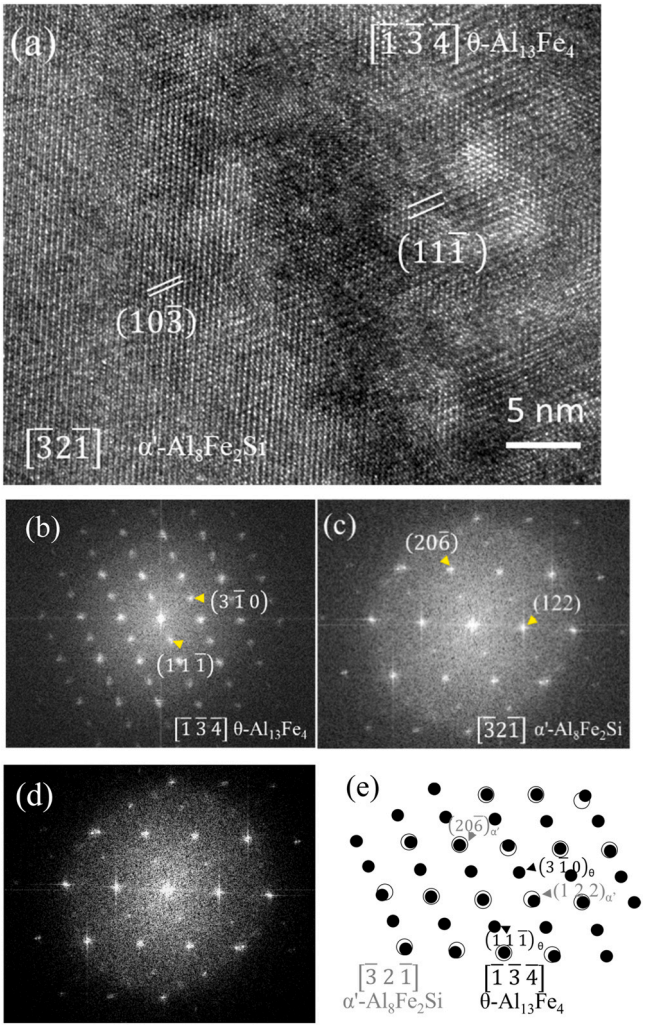

Fig. 5. (a) High-resolution TEM (HRTEM) image showing the interface between α'-Al_8Fe_2Si phase and θ-$Al_{13}Fe_4$ phase, and fast Fourier transformation (FFT) patterns of (b) θ-$Al_{13}Fe_4$ with the incident electron beam paralleled to [$\bar{1}$ 3 $\bar{4}$] zone direction and (c) α'-Al_8Fe_2Si with the incident electron beam paralleled to [$\bar{3}$ 2 $\bar{1}$] zone direction, (d) the FFT containing both α'-Al_8Fe_2Si phase and θ-$Al_{13}Fe_4$ phase, and (f) the schematic indexed FFT of (d) viewed along the zone direction of [$\bar{1}$ 3 $\bar{4}$] of θ-$Al_{13}Fe_4$ and [$\bar{3}$ 2 $\bar{1}$] of α'-Al_8Fe_2Si showing the orientation relationship between α'-Al_8Fe_2Si and θ-$Al_{13}Fe_4$.

several different pairs of zone directions during the TEM analysis. Some examples with lower indexed zone directions will be presented here.

The HRTEM image, Fig. 5a, shows the interface between θ-$Al_{13}Fe_4$ and α'-Al_8Fe_2Si when viewed along the zone direction of [$\bar{1}\bar{3}\bar{4}$]of θ-$Al_{13}Fe_4$ and [$\bar{3}2\bar{1}$] of α'-Al_8Fe_2Si. The interface is not sharp, and some transition area can be observed at the interface. The fast Fourier transformation (FFT) patterns of α'-Al_8Fe_2Si phase and θ-$Al_{13}Fe_4$ phase are shown in Fig. 5b-c. The FFT pattern (Fig. 5d) containing both phases and its indexed pattern (Fig. 5e) reveal an orientation relationship (OR) between α'-Al_8Fe_2Si and θ-$Al_{13}Fe_4$: (10$\bar{3}$) [$\bar{3}2\bar{1}$] α'-Al_8Fe_2Si // (11 $\bar{1}$) [$\bar{1}\bar{3}\bar{4}$] θ-$Al_{13}Fe_4$.

The TEM-EDX composition of θ-$Al_{13}Fe_4$ in Al-4Fe-4Si contains 2.7 ± 0.2 at% Si, and 20.6 ± 0.5 at% Fe, and the composition of α'-Al_8Fe_2Si is 10.4 ± 0.1 at% Si, and 15.3 ± 0.1 at% Fe. The lattice parameters of θ-$Al_{13}Fe_4$ measured with single crystal X-ray was 15.424 Å (*a*), 8.052 Å (*b*), 12.404 Å (*c*), with 107.7° (β). The lattice parameters of α'-Al_8Fe_2Si measured with TEM was 12.13 Å (*a*), 12.13 Å (*b*), 26.68 Å (*c*).

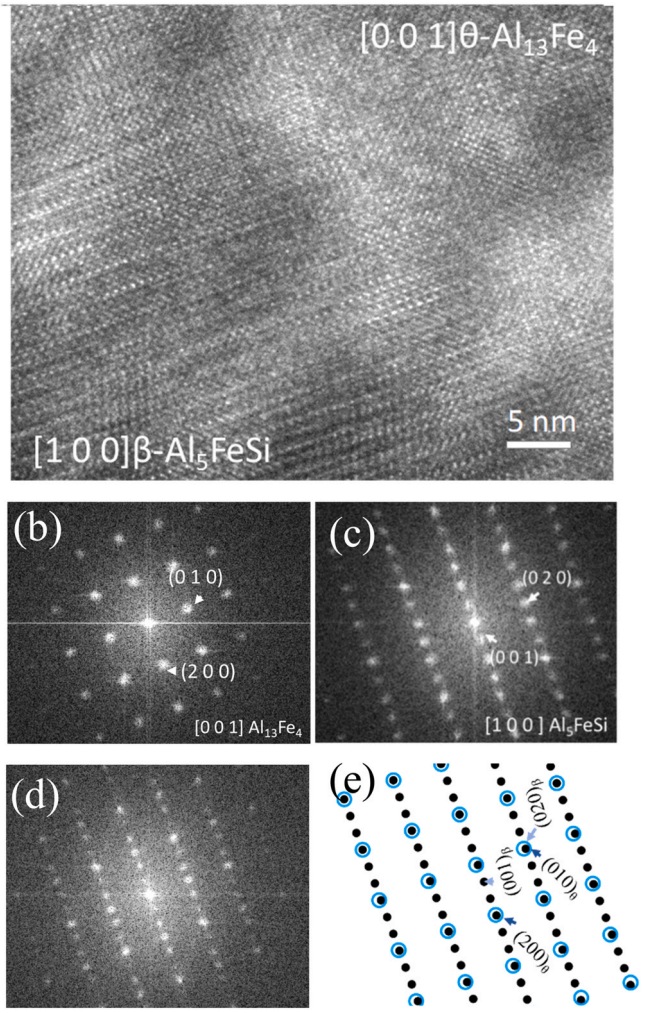

Fig. 6. Interface between β-Al_5FeSi/θ-$Al_{13}Fe_4$, (a) High-resolution TEM (HRTEM) image showing the interface between β-Al_5FeSi phase and θ-$Al_{13}Fe_4$ phase in Al-4Si-4Fe alloy, and fast Fourier transformation (FFT) patterns of (b) β-Al_5FeSi phase and (c) θ-$Al_{13}Fe_4$ phase, and (d) FFT pattern containing both β-Al_5FeSi and θ-$Al_{13}Fe_4$ phase, (e) the schematic representation of the indexed FFT of (d) viewed along the zone direction of [0 0 1] of θ-$Al_{13}Fe_4$ and [1 0 0] of β-Al_5FeSi showing the orientation relationship between β-Al_5FeSi and θ-$Al_{13}Fe_4$.

The HRTEM image, Fig. 6a, shows the interface between θ-$Al_{13}Fe_4$ and β-Al_5FeSi when viewed along the zone direction of [001] of θ-$Al_{13}Fe_4$ and [100] of β-Al_5FeSi. The interface is again a diffuse interface, and a transition area can be observed at the interface, suggesting continuous incorporation of Si into the structure. The fast Fourier transformation (FFT) patterns of β-Al_5FeSi phase and θ-$Al_{13}Fe_4$ phase are shown in Fig. 6b-c. The FFT patterns containing both phases are shown in Fig. 6d. The schematic diagram showing the indexed FFT of Fig. 6d is in Fig. 6e. These results indicate an OR between θ-$Al_{13}Fe_4$ and β-Al_5FeSi to be: (020) [100] β-Al_5FeSi // (010) [001] θ-$Al_{13}Fe_4$. The TEM-EDX result, Table 2, shows that the β-Al_5FeSi contains 16.9 ± 0.1at% Si, which is higher than that of θ-$Al_{13}Fe_4$ (2.7 ± 0.2 at% Si) and α'-Al_8Fe_2Si (10.4 ± 0.1 at% Si).

3.3. θ-$Al_{13}Fe_4$ in Al-1Fe-1Si (−3.7Ti-1.5B) alloy

The phase transformation between θ-$Al_{13}Fe_4$ and AlFe in Al-1Fe-1Si alloy containing TiB_2 particles was investigated to understand the effect of heterogeneous sites for nucleation on the choice of FIMC. The SEM-SE (secondary electron) image, Fig. 7, shows the microstructure of Al-1Si-1Fe(−3.7Ti-1.5B) alloy with 0.4 wt% free Ti solidified at 1 K/s, indicating a microstructure with a mixture of

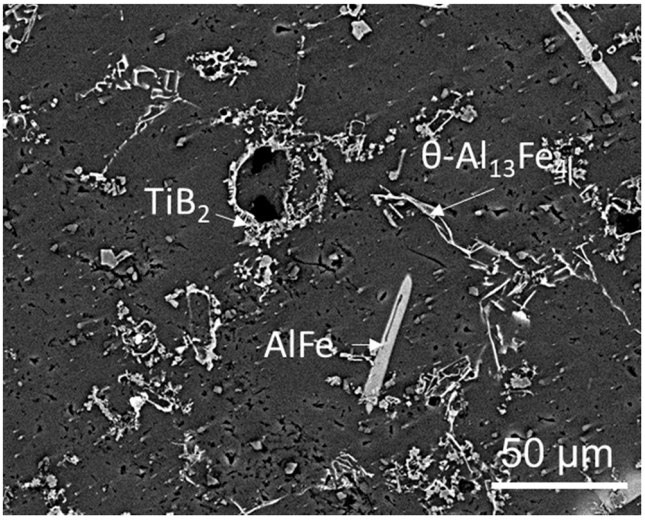

Fig. 7. SEM-SEI image showing the microstructure of Al-1Si-1Fe(−3.7Ti-1.5B) alloy which solidified at 1 K/s, indicating a microstructure of some mixed FIMCs.

FIMCs. The TiB_2 particles agglomerations distribute randomly in the Al grains or at the grain boundary. Some larger FIMC particles with long plate-like or needle-like morphology distribute in the Al grains, which can be considered as primary FIMCs. This FIMC was identified as AlFe which has B2-CsCl structure via TEM analysis. The AlFe phase observed here is not expected according to the Al-Fe phase diagram calculations. We expect localised inhomogeneities in the liquid composition and the presence of TiB_2 particles may promote this phase. The phase transformation from AlFe to θ-$Al_{13}Fe_4$ observed in this alloy illustrates the instability of this phase. Some smaller plate or needle-like FIMCs distribute at the grain boundaries, which are likely to be FIMCs in the eutectic structures. These FIMC in the eutectic structure was identified as θ-$Al_{13}Fe_4$ phase with TEM analysis. AlFe phase is rarely reported in cast Al alloys. In addition, a phase transformation was observed at the surface of AlFe with TEM, and a well-defined OR was identified and shown in Fig. 8.

The bright field TEM image, Fig. 8a, shows the needle-like central AlFe phase with the θ-$Al_{13}Fe_4$ phase at the surface. The TEM-EDX results, Table 2, show that the AlFe contains 1.5 ± 0.1at% Si, and the θ-$Al_{13}Fe_4$ contains 2.4 ± 0.1at% Si. The Si is likely to be continuously incorporated into AlFe phase during the solidification progresses, and the phase transformation occurs from AlFe to θ-$Al_{13}Fe_4$ through a reaction: L + AlFe → θ-$Al_{13}Fe_4$ + α-Al.

The SAED patterns from AlFe, θ-$Al_{13}Fe_4$ and from a region containing both phases are shown in Fig. 8b-d, when viewed along the [112] zone direction of AlFe and [100] θ-$Al_{13}Fe_4$, respectively. Fig. 8e shows the schematic illustration of the SAED in Fig. 8d. The HRTEM image, Fig. 8f, shows the interface between AlFe and θ-$Al_{13}Fe_4$. Many planar defects can be observed on the θ-$Al_{13}Fe_4$ phase. The interface between the two phases reveals an orientation relationship of $(1\bar{1}\bar{1})$AlFe// (001) θ-$Al_{13}Fe_4$, and [112] AlFe// [100] θ-$Al_{13}Fe_4$.

3.4. θ-$Al_{13}Fe_4$ in Al-Fe-Mn-Si-Mg alloys

The phase transformation between θ-$Al_{13}Fe_4$ and the α-$Al_{15}(Fe,Mn)_3Si_2$ was observed in Al-5Mg-2Si-0.6Mn-1.3Fe alloy. The Al alloy in this work had a composition of 5.1 ± 0.5Mg, 2.0 ± 0.3 Si, 0.6 ± 0.1 Mn and 1.3 ± 0.05 Fe (in wt%) with Al balance. The phase diagram of the Al-5Mg-2Si-0.6Mn-*x*Fe system was calculated with the Pandat software and its associated Al-database as shown in Fig. 12c. It shows that the α-$Al_{15}(Fe,Mn)_3Si_2$ is calculated as primary equilibrium phase. The as-cast microstructure of this alloy solidified at 3.5 K/s is shown in Fig. 9. The formation of FIMCs in this alloy is

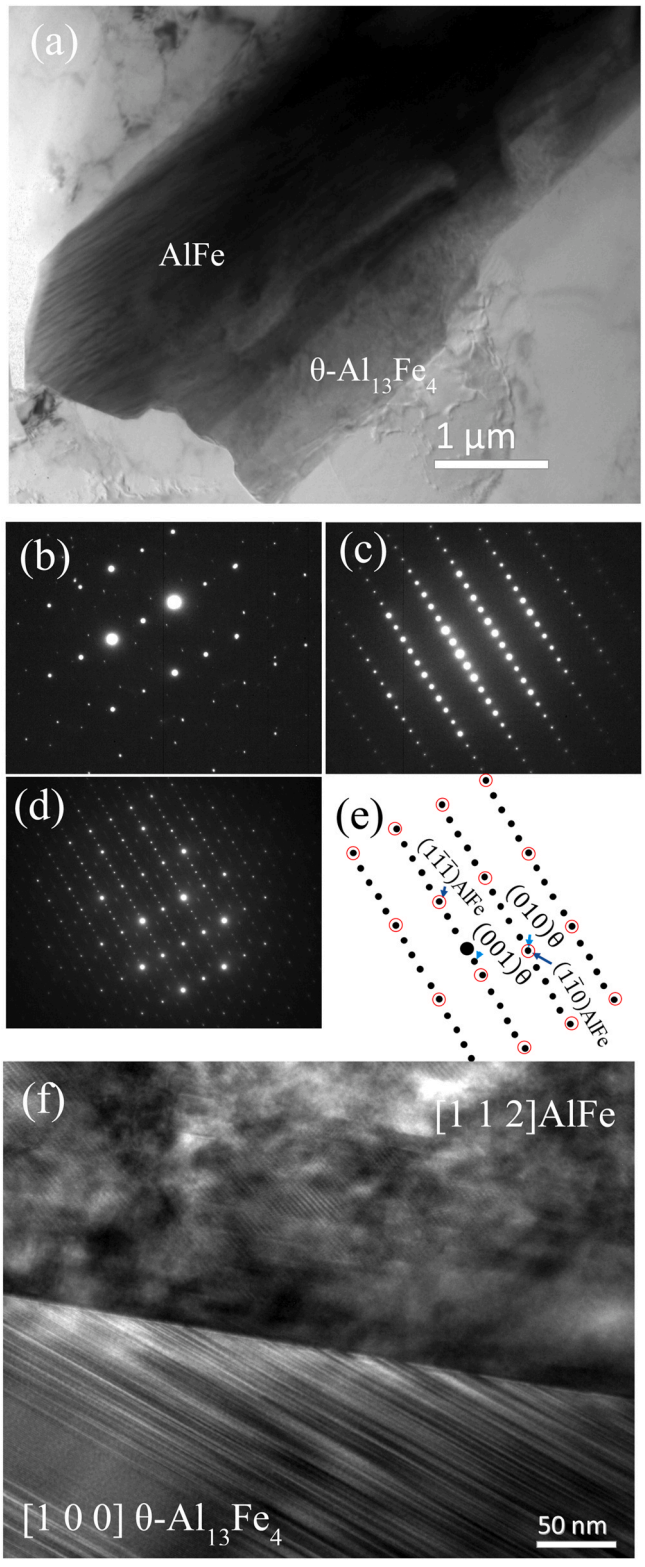

Fig. 8. (a) Bright field TEM image of interface of interface of AlFe/ θ-$Al_{13}Fe_4$, and the SAED patterns when (b) viewed along the zone direction of [1 0 0] θ-$Al_{13}Fe_4$, and (c) viewed along the zone direction of [1 1 2] AlFe, (d) and (e) the SAED patterns and corresponding indexed pattern of (d) containing both AlFe and θ-$Al_{13}Fe_4$, and (f) HRTEM image of interface of AlFe/ θ-$Al_{13}Fe_4$ showing an orientation relationship of (1$\bar{1}\bar{1}$) AlFe// (0 0 1) $Al_{13}Fe_4$, and [1 1 2] AlFe// [1 0 0] θ-$Al_{13}Fe_4$.

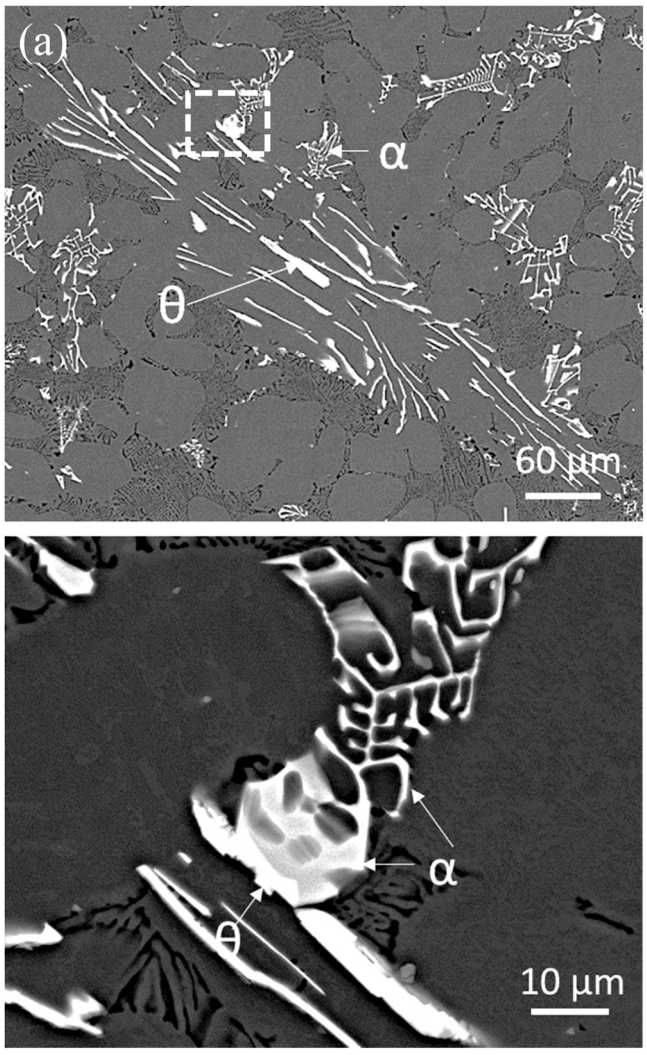

Fig. 9. Microstructure of (a) Al-5Mg-2Si-0.6Mn-1.3Fe alloy which solidified at 3.5 K/s, indicating a microstructure of some mixed θ- $Al_{13}Fe_4$ + α-Al) and (α-Al_{15}(Fe, Mn)$_3Si_2$ + α-Al) eutectic, and (b) high magnification SEM-BSE image of the frame in (a) indicate that the plate-like θ- $Al_{13}Fe_4$ phase transformed into the other FIMCs with the compact morphology.

complicated and the details has been reported in pervious contribution [22]. The SEM-BSE image, Fig. 9a, shows that in this sample, the FIMCs are mainly in plate-like and Chinese script morphologies. The high magnification SEM observation on the local area marked in Fig. 9a is shown in Fig. 9b. The compacted grey particles (α-Al_{15}(Fe,Mn)$_3Si_2$) which leading a Chinese script morphology FIMC connects and grows from the plate-like FIMC (θ-$Al_{13}Fe_4$). The calculated phase diagram, Fig. 12c, shows that the equilibrium primary phase of Al-5Mg-2Si-0.7Mn-1.2Fe alloy supposed to be α-Al_{15}(Fe,Mn)$_3Si_2$, but not θ-$Al_{13}Fe_4$. However, due to the smaller nucleation undercooling [20], the θ-$Al_{13}Fe_4$ nucleated firstly on the native $MgAl_2O_4$ particles [22], and transformed into α-Al_{15}(Fe,Mn)$_3Si_2$ via a reaction: L + θ-$Al_{13}Fe_4$ → α-Al_{15}(Fe,Mn)$_3Si_2$ + α-Al.

The interface between θ-$Al_{13}Fe_4$ and α-Al_{15}(Fe,Mn)$_3Si_2$ was investigated with TEM, Fig. 10. A well-defined OR between these two phases was identified. The dark field TEM image, Fig. 10a, shows the interface between θ-$Al_{13}Fe_4$ and α-Al_{15}(Fe,Mn)$_3Si_2$ when viewed along the [010] zone direction of θ-$Al_{13}Fe_4$. Some nano-scaled size α-Al can be seen from the α-Al_{15}(Fe,Mn)$_3Si_2$, which indicates the alloy elements diffusion during the phase transformation. The HRTEM image containing both θ-$Al_{13}Fe_4$ and α-Al_{15}(Fe,Mn)$_3Si_2$ are shown in Fig. 10b [22]. The corresponding schematic indexed FFT patterns is shown in Fig. 10c [22]. The results reveal an orientation relationship between θ-$Al_{13}Fe_4$ and α-Al_{15}(Fe, Mn)$_3Si_2$: ($\bar{2}$01) θ-$Al_{13}Fe_4$ // 2.3°

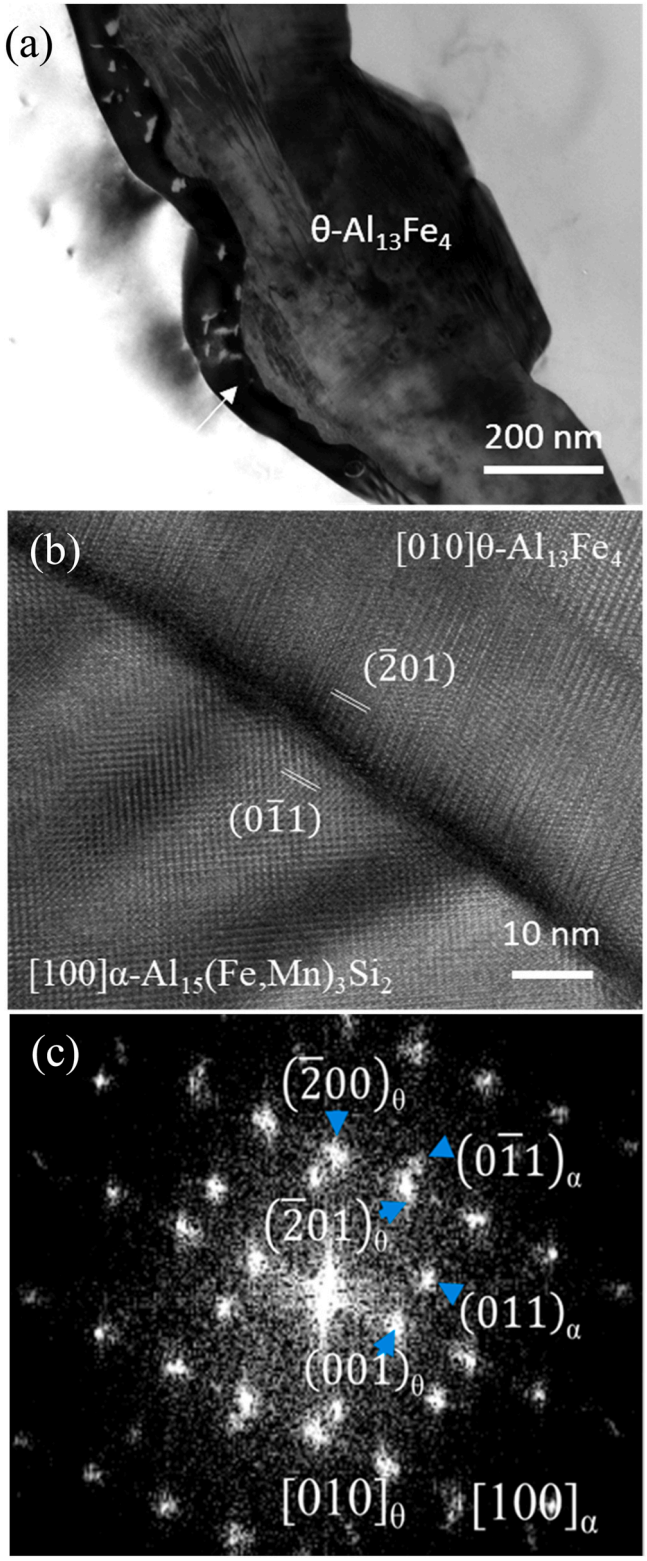

Fig. 10. (a) Dark field TEM image showing the interface between θ-$Al_{13}Fe_4$ and α-Al_{15}(Fe, Mn)$_3Si_2$showing some nano-meter size α-Al grains in α-Al_{15}(Fe, Mn)$_3Si_2$, and (b) the HRTEM image of the interface between θ-$Al_{13}Fe_4$/ α-Al_{15}(Fe, Mn)$_3Si_2$ viewed along the [0 1 0] zone axis of θ-$Al_{13}Fe_4$ and (c) the indexed FFT patterns showing the orientation relationship between θ-$Al_{13}Fe_4$ and α-Al_{15}(Fe, Mn)$_3Si_2$: ($\bar{2}$ 0 1) θ-$Al_{13}Fe_4$ // 2.3° (0 $\bar{1}$ 1)α-Al_{15}(Fe, Mn)$_3Si_2$, and [0 1 0] θ-$Al_{13}Fe_4$ // [1 0 0] α-Al_{15}(Fe, Mn)$_3Si_2$.

(0$\bar{1}$1)α-Al_{15}(Fe, Mn)$_3Si_2$, and [010] θ-$Al_{13}Fe_4$ [100] α-Al_{15}(Fe, Mn)$_3Si_2$. In addition, the TEM-EDX result, Table 2, shows that in this alloy, not only Si (1.8 ± 0.1 at%), but also Mn (6.4 ± 0.1 at%) can incorporate into θ-$Al_{13}Fe_4$ phase in Al-5Mg-2Si-0.7Mn-1.2Fe alloy, which requires further investigation.

3.5. First principles calculation and related thermodynamics for the FIMCs

The experimental results revealed that the phase transformation between different types of FIMCs is a diffusion-controlled process. During the phase transformation, the vital element which determinate different phase transformation reactions is Si. Each FIMC has significant difference in Si concentration, Table 2. Therefore, the difference in crystal structure and the atomic sites of these FIMCs were investigated based on the reported structural models [3,24,25,38]. The solubility of Si in and phase stability of different FIMCs are compared based on the structural models in the literature, Table 4. Further to that, the solubility of Si using different structural models were calculated and compared to the experimentally measured Si concentration.

The solubility of Si in different FIMCs based on the above crystal structural models were calculated and shown in Table 4. It shows that the Si solubility in FIMCs has a sequence as: β-Al_5FeSi (15.38 at. %) > α'-Al_8Fe_2Si (9.80 at.%) > α-Al_{15}(Fe, Mn)$_3Si_2$ (7.68 at.%) > θ-$Al_{13}Fe_4$ (4.9 at.%). The Si concentration in θ-$Al_{13}Fe_4$ (4.9%) compound is based on the compound model calculated with DFT. As shown in Table 4, the Si concentrations in compounds α'-Al_8Fe_2Si, β-$Al_{4.5}$FeSi_I and α-Al_{15}(Fe, Mn)$_3Si_2$ are based on the compound models calculated from the literatures [3,25,38] which based on the experimental compound compositions. The Si concentrations in compound β-$Al_{4.5}$FeSi_II and β-$Al_{4.375}FeSi_{1.125}$_III is based on the First-principles calculation done in this work. Our measured experimental Si concentrations in different types of FIMCs using TEM-EDX shows the same trend in the amount of Si incorporated into the structures as those of the calculated Si concentrations sequence. There is a significantly large gap between the maximum Si concentrations determined purely on DFT calculation and the experimentally measured Si solubility in FIMCs. Our experimental result shows that a 2.7 at% Si is incorporated into θ-$Al_{13}Fe_4$, but the result from crystal structural model calculated with DFT is up to 4.9 at% [24]. The DFT calculation reveals a theorical possibility of Si concentration in compounds regardless of phase stability, which can provide some valuable information for the further investigation. Further studies are going to continue to build new crystal structural models for the other FIMCs using DFT calculations.

Both experimental and theoretical efforts have been made to obtain structural models for the FIMCs investigated. Experimental evidence revealed the complexity of crystal structures with partial occupation and/or multiple atomic species occupations at the Wyckoff sites in these FIMCs. This provides extra freedom for the crystals, Table 4. The primary FIMCs form at elevated temperatures during casting. At high temperature, the extra freedom at the atomic sites becomes an important factor in determining the relative stability of the FIMCs. To obtain a further insight into the crystal chemistry of the Fe-IMCs, parameters-free first-principles methods have been used [24,39–41]. The first-principles calculations have been conducted to investigate the Si solution in FIMCs including θ-$Al_{13}Fe_4$ [24] and β-$Al_{5.5}Fe$ [41]. The calculated results are summarized in Fig. 11. The β-$Al_{5.5}Fe$ has higher formation energy compared with θ-$Al_{13}Fe_4$, in agreement with the experimental observations that the θ-phase is the stable phase whereas the β-phase is not in the binary Fe-Al phase diagram. At low temperatures, the most stable configuration is θ-$Al_{5.69}(Si^{IX})_{0.31}Fe_4$ containing 3.92 at% of Si [24].

First-principles calculation, Fig. 11b, reveals that a high concentration of Si goes into solution in β-phase and the configuration of the highest stability with respect to the elemental Al, Si and Fe is when A11 sites (β-$Al_{4.5}Si^{I}$ Fe) or Al6 site (β-$Al_{4.5}Si^{VI}$ Fe) which contains 15.38 at% Si, are fully occupied by Si at the ambient conditions

Table 4
Structural models and related configurational entropy contributions in the intermetallic compounds. The definition of C(Si) = *N*(Si)/[*N*(Si) + *N*(Al) + *N*(Fe) + *N*(Mn)].

Compound	Lattice	N_{atoms}	$N_{species}$ / N_{atom}	Structural formula	C (Si) at%
θ-$Al_{13}Fe_4$	Monoc.	102	Al: 15 / 73 Si: 2 / 5 Fe: 5 /24	θ-$Al_{70}(Al_{0.375}Si_{0.625})_8Fe_{24}$ &θ-$(Al_{0.0641}Si_{0.9359})_{78}Fe_{24}$	4.90%[24]
α'-Al_8Fe_2Si	Hex.	238.288	Al:14 /168.912 Si: 4 /23.376 Fe: 5 / 46	Al_{168} $(Al_{0.152})_6$ $Si_{18}(Si_{0.848})_6(Si_{0.144})_2Fe_{46}$	9.80%[25]
β-$Al_{4.5}FeSi$_I	Monoc.	52	Al: 6 / 36 Si: 6 / 8 Fe: 1 / 8	$(Al_{9/11}Si_{2/11})_{44}Fe_8$	15.38%[38]
β-$Al_{4.5}FeSi$_II	Monoc. This work	52	Al: 5 / 36 Si: 1 / 8 Fe: 1 / 8	$Al_{36}Si^{I}_{8}Fe_8$	15.38 (This work)
β-$Al_{4.375}FeSi_{1.125}$_III	Monoc. This work	52	Al: 5 / 35 Si: 1 / 8 + 6/1 Fe: 1 / 8	$Al_{35}Si_1$ Si^{I}_{8} Fe_8	17.3 (This work)
α-$Al_{15}(Fe,Mn)_3Si_2$	BCC	138	Al: 9/100.89 Si: 9/10.602 Fe: 2/21.240 Mn: 10/5.268	$(Al_{0.885}Si_{0.093}Mn_{0.022})_{114}$ $Fe_{12}(Fe_{0.77}Mn_{0.23})_{12}$	7.68%[3]

Note, N means the number of atoms, e.g. N(Si) for number of Si atoms. C(Si) represent for the concentration (at%) of Si.

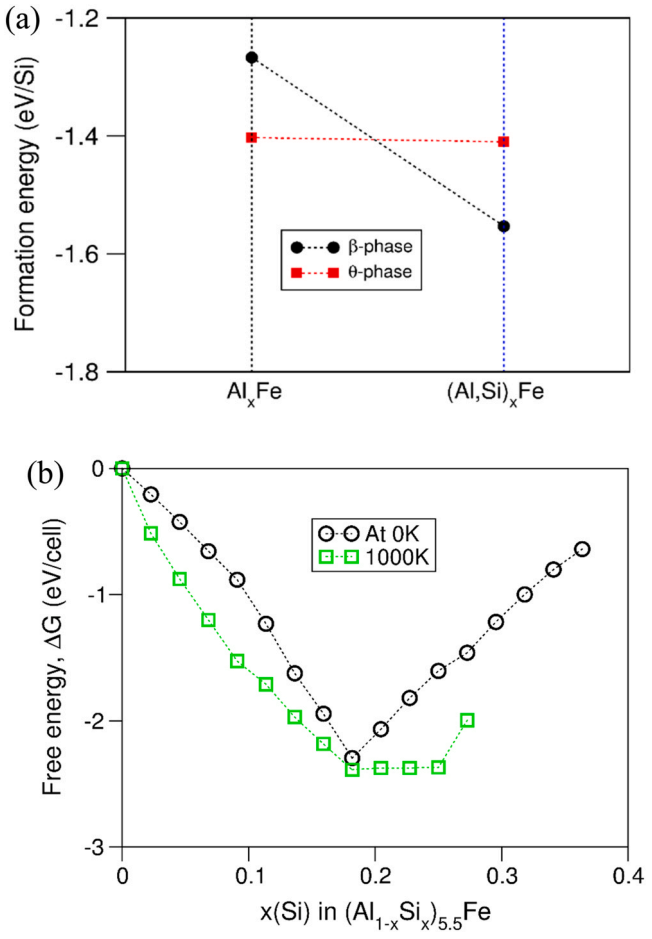

Fig. 11. (a)The dependence of the formation energies of the θ-$Al_{13}Fe_4$ [24] and β-$Al_{5.5}Fe$ phases (Al_xFe) on Si substitution using first principles calculation. The chemical formula for the Si substitution phase with higher stability are θ-$(Al_{0.94878}Si^{IX}_{0.05128})_{13}Fe_4$ and β-$Al_{4.5}Si^{I}$ Fe, here the Romans numerals represent atomic (Al) sites in [6] and [38], respectively; and (b) the dependences of free energies of the β-phase on Si contents at 0 K and 1000 K.

[39]. The first-principles calculations also showed that addition of more Si to the configurations of high stability at ambient condition, e.g. (β-$Al_{4.5}Si^{I}$ Fe) may increase the formation energy, but it also increases the number of configurations significantly. At 1000 K the β-phase has 15.38–21.15 at% Si content [39], whereas the Si content in the θ-phase is between 2.94 at% and 4.90 at% due to the configuration entropy contributions [24]. This indicates that the Si concentration in the Fe-IMCs depends on the chemical compositions of the alloy and the casting process.

4. Discussion

4.1. Heterogeneous nucleation effects on phase transformation of θ-$Al_{13}Fe_4$

In this study, 5 different Al-Fe alloys were investigated, where θ-$Al_{13}Fe_4$ phase formed during solidification as a primary intermetallic or as an intermetallic in the eutectic structure. Multiple types of phase transformation were observed in corresponding samples from θ-$Al_{13}Fe_4$ to the other types of FIMCs. The θ-$Al_{13}Fe_4$ in Al-1Fe-1Si, Al-4Fe-4Si alloys was calculated as equilibrium phase using Pandat software based on Scheil solidification model to illustrate the 2D vertical-sections at given alloy chemistry with varying Si concentrations, Fig. 12a-b. The $Al_{13}Fe_4$ in other alloys such as Al-5Mg-2Si-0.7Mn-1.2Fe alloy was calculated to be a non-equilibrium phase, Fig. 12c. However, during the casting process, the phase selection of the FIMCs can be different to that calculated phases due to the non-equilibrium phase selections [11,21,22]. The changes to phase selection during the solidification process will cause the non-equilibrium phase transformation and solidification sequence. For example, the $Al_{13}Fe_4$ formed in place of the equilibrium α-Al_{15}(Fe, Mn)$_3Si_2$ phase in Al-5Mg-2Si-0.7Mn-1.2Fe alloy and then transformed into equilibrium α-Al_{15}(Fe, Mn)$_3Si_2$ during further cooling. The AlFe formed first instead of the equilibrium θ-$Al_{13}Fe_4$ phase in Al-1Fe-1Si(−3.7Ti-1.5B) alloy and then transformed into the equilibrium θ-$Al_{13}Fe_4$. The most complicated case is the FIMCs formation in the Al-4Fe-4Si alloy, Fig. 12b. Multiple primary FIMCs such as θ-$Al_{13}Fe_4$ and α'-Al_8Fe_2Si formed (Fig. 4a), and multiple types of phase transformation between θ-$Al_{13}Fe_4$ and the other types of FIMCs such as α'-Al_8Fe_2Si, β-Al_5FeSi were observed. The solidification sequence and the complicated transformation sequence was presented in detail in a separate contribution [45].

The previous research [11,21,22,32–34] showed that the formation of FIMCs during the solidification is very sensitive to the alloy compositions, solidification conditions etc., which can easily be changed. Many types of phase transformation between different types of FIMCs have been reported in different alloys under different casting conditions. Recent research reported [20,22,49] that the

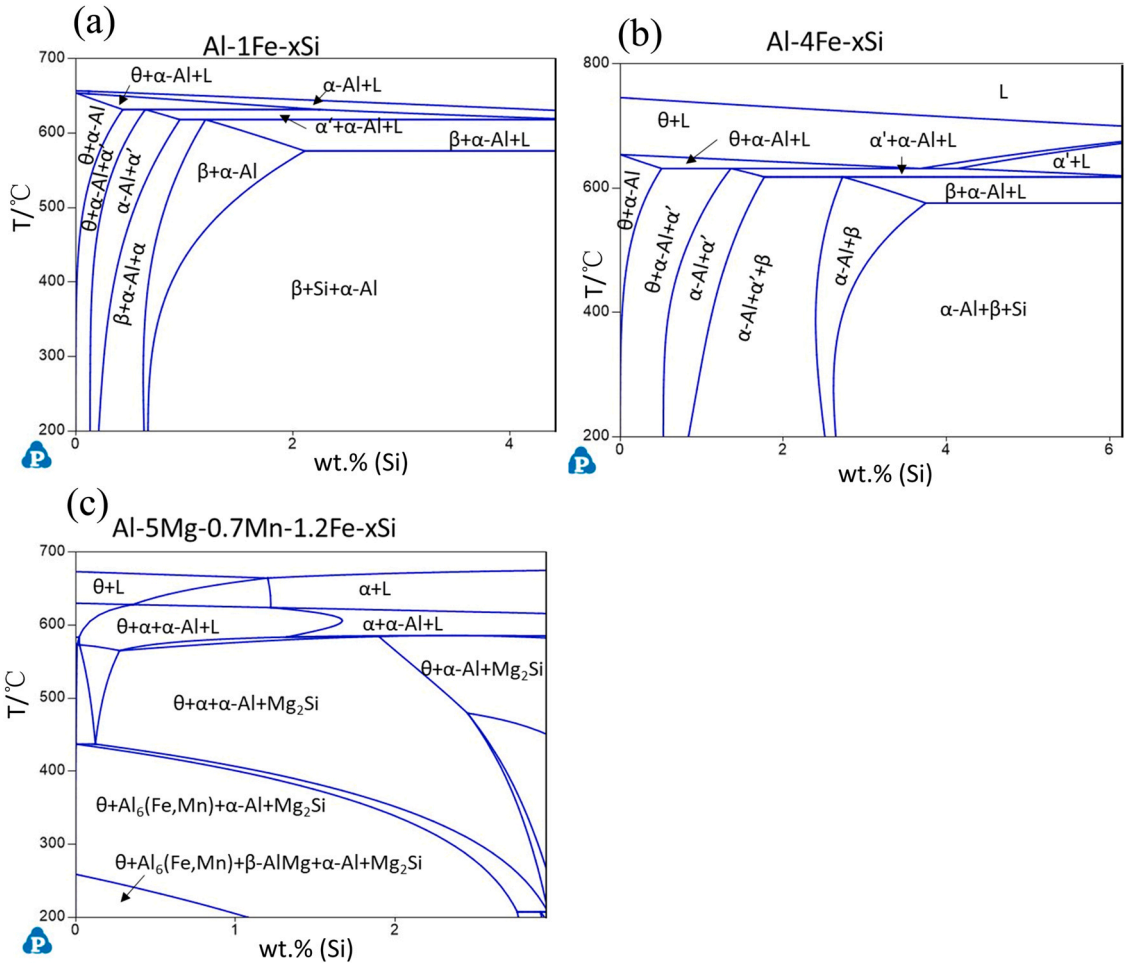

Fig. 12. Calculated phase diagrams of (a) Al-1Fe-*x*Si, (b) Al-4Fe-*x*Si, (c) Al-5Mg-0.7Mn-1.2Fe-*x*Si. Note: the θ is θ-$Al_{13}Fe_4$, α' is Al_8Fe_2Si, β is Al_5FeSi, α is $Al_{15}(Fe, Mn)_3Si_2$.

variations in phase selection among these FIMCs is due to the difficulties associated with nucleation which required multiple constitutive elements and large undercooling. It also shows that the θ-$Al_{13}Fe_4$ requires smaller number of elements and smaller nucleation undercooling compared to the other types of common FIMCs in as-cast Al alloys. This is likely why it is easier to form θ-$Al_{13}Fe_4$ in Al alloys such as Al-5Mg-2Si-0.7Mn-1.2Fe than the calculated equilibrium α-$Al_{15}(Fe, Mn)_3Si_2$ phase. The other factors such as the TiB_2 can also change the phase selection of FIMCs. In this study, the Al-1Fe-1Si alloy containing TiB_2 particles and 0.4% free Ti promoted a metastable AlFe phase formation in place of θ-$Al_{13}Fe_4$. The non-equilibrium AlFe phase is not stable in the alloy and subsequently transformed into θ-$Al_{13}Fe_4$. It is reported [20,42,43] that the additional elements in the Al-Ti-B master alloys can change the interfacial segregation on the TiB_2 interface, which therefore changed the nucleation potency of these TiB_2 particles and promote the formation of one phase over another.

4.2. Effects of Si on the crystal structural of θ-$Al_{13}Fe_4$ and β-phase

Structurally, θ-$Al_{13}Fe_4$ has a large range of crystal chemistries due to Si and transition metal incorporation. It has a monoclinic lattice with space group C2/m [6,44]. There are 20 crystallographically distinct atomic sites (5 Fe and 15 Al) and 102 atoms in total in a unit cell [6]. A recent work [24] on the calculation of the Si solution in θ-$Al_{13}Fe_4$ phase using first-principles density-Functional Theory (DFT) showed that it is energetically favorable for Si to replace some Al in specific sites in θ-$Al_{13}Fe_4$, but Si substitution into the Fe sites is very unlikely due to the high energy associated with this. It showed that the increased energy associated with Si substitution on 2 Al sites (Al8 and Al9) is negative, and on the other 2 sites (Al6 and Al4) is less favourable with but with very minor increase in energy. It also revealed that partial replacements of Al by Si at these sites break the local symmetry of the crystal, resulting in a localised triclinic structure compared with the global monoclinic structure.

In this study, the lattice parameters of θ-$Al_{13}Fe_4$ without and with Si incorporation in different Al alloys were measured and shown in Table 3, and the corresponding compositions of θ-$Al_{13}Fe_4$ particles were measured and listed in Table 2. The X-ray diffraction patterns for the single crystals revealed the lattice parameters: a = 15.4824(3) Å, b = 8.08146(15) Å, c = 12.4689(3) Å and β = 107.689(2) ° for a single crystal without Si, θ-$Al_{13}Fe_4$; and a = 15.44239(11) Å, b = 8.0521(5) Å, c = 12.4040(8) Å and β = 107.649(7) ° for a single crystal with Si, θ-$(Al_{1-x}Si_x)_{13}Fe_4$ with x = 0.024. The results showed the crystal structure of θ-$Al_{13}Fe_4$ remains monoclinic, although the Si substitutes in θ-$Al_{13}Fe_4$ phase with a concentration is up to 2.7at%. The experimental results in this work revealed that the lattice parameters and cell volume of θ-$Al_{13}Fe_4$ decreases with the increase of Si concentration. This is supported by the DFT calculation [24]. After increased amount of Si atoms diffused into θ-$Al_{13}Fe_4$ crystals, more Al sites were replaced with Si and the symmetry of θ-$Al_{13}Fe_4$ crystal was gradually changed and finally transformed into the other types of FIMCs.

Both the calculation and the experimental results indicated that Si can go into θ phase but only up to a given concentration. Our calculation results shown in Fig. 11 revealed that the FIMCs became unstable when the Si concentration reach their solubility. Therefore,

the Si concentration of FIMCs at the interface that phase transformed to the other types of FIMCs can be considered as their maximum solubility. For example, during the multi-step phase transformation from θ to α', α' to β, and β to δ, the solubility of Si in these FIMCs can be considered as 2.7 at% of θ, 10.4 at% of α', and 16.9 at% of β, respectively. The solubility of Si in different FIMCs can change with the experimental conditions such as temperature at which the phases transformation can occur. Further investigation is required to understand the relationship between the alloy composition, concentration of Si in the FIMC and phase stability.

Recent research [21] showed that the phase transformation among different types of FIMCs are diffusion controlled. Therefore, which types of FIMCs form through phase transformation from θ-$Al_{13}Fe_4$ depends on many factors such as alloy composition, cooling rate. Additionally, a few pairs of ORs between θ and the other FIMCs, α', β were identified. These ORs contains some crystallographic information of the structure transition between these FIMCs. Further investigation is working.

The calculation results also revealed that the chemical composition of β-phase is $Al_{4.5}FeSi$, which is similar as the experimental observation [38]. However, the Si distribution is different from that reported previously. The experimental model suggested a homogeneous distribution of Si at the Al sites, whereas the first-principles calculations predicted that the Si atoms are at either the Al1 or the Al6 site. Additionally, the DFT simulation also showed a high configurational entropy contribution for increased Si solution in the β-phase. This indicates that at high temperature (> 700 K), the β-phase may contain more Si than the configuration of stable structure at ambient conditions [41].

4.3. Effects of thermodynamic on phase transformation of θ-$Al_{13}Fe_4$

Naturally, the chemical composition has an impact on the formation of θ-$Al_{13}Fe_4$ phase in Al alloys. The concentration of Si in the θ-$Al_{13}Fe_4$ phase depending on the chemical composition in the Al alloys and casting conditions. The details of phase transformation mechanisms between different types of FIMCs have been reported in our recent contributions [21]. It is reported that these phase transformations between various FIMCs are diffusion-controlled. The phase transformation of FIMCs from θ-$(Al,Si)_{13}Fe_4$ with a low Si concentration to other FIMCs with a higher Si content (such as α'-Al_8Fe_2Si, α-$Al_{15}(Fe,Mn)_3Si_2$, β-Al_5FeSi) depends on the Fe and Si diffusion at high temperature and long holding times. The TEM-EDX results from various FIMCs observed in this study, Table 2, showed that the Fe content decreased, and the Si content increased in each of the FIMC as the phase transformation sequence progressed from θ-$Al_{13}Fe_4$ to α-$Al_{15}(Fe, Mn)_3Si_2$, α'-Al_8Fe_2Si and β-Al_5FeSi. The experimentally measured Si concentration in Table 2 revealed a sequence among different types of FIMCs as: $C_{\theta}^{Si} < C_{\alpha}^{Si} < C_{\alpha'}^{Si} < C_{\beta}^{Si}$. The experimental results in this study showed a complicated phase selection and the variable following phase transformations depending on the alloy composition, which illustrated that in high Si containing Al alloys, at certain casting conditions, especially at slow solidification process. The FIMCs such as α'-Al_8Fe_2Si, α-$Al_{15}(Fe,Mn)_3Si_2$, β-Al_5FeSi with higher Si content is more stable than those with a lower Si content FIMCs such as θ-$Al_{13}Fe_4$, indicating the possible thermodynamic stability of these phases at the investigated alloys. However, the final microstructure selection was resulted from the effects of multiple factors, such as thermodynamic, nucleation difficulty, etc.

5. Conclusions

(1) The experimental measured lattice parameters (*a*, *b*, *c*) of θ-$Al_{13}Fe_4$ decrease with the increasing Si concentration in θ-$Al_{13}Fe_4$ particles formed in different Al alloys. However, the maximum Si concentration doped in θ-$Al_{13}Fe_4$ measured from experimental results is lower than that of calculation.

(2) Multi types of phase transformation between θ-$Al_{13}Fe_4$ and the other types of FIMCs were observed in Al-Fe-Si alloys.
   1) L + θ-$Al_{13}Fe_4$ → α'-Al_8Fe_2Si+ α-Al
   2) L + θ-$Al_{13}Fe_4$ → β-Al_5FeSi+ α-Al
   3) L + AlFe→ θ-$Al_{13}Fe_4$ + α-Al
   4) L + θ-$Al_{13}Fe_4$ → α-$Al_{15}(Fe,Mn)_3Si_2$ + α-Al

(3) The orientation relationships between $Al_{13}Fe_4$ and the other types of FIMCs were well-defined.

A. $(10\bar{3})$α'-Al_8Fe_2Si // $(11\bar{1})$ θ-$Al_{13}Fe_4$, and $[\bar{3}2\bar{1}]$ α'-Al_8Fe_2Si //$[\bar{1}\bar{3}\bar{4}]$ θ-$Al_{13}Fe_4$
(020) β-Al_5FeSi // (010) θ-$Al_{13}Fe_4$, and [100] β-Al_5FeSi // [001] θ-$Al_{13}Fe_4$
B. $(1\bar{1}\bar{1})$ AlFe// (001) θ-$Al_{13}Fe_4$, and [112] AlFe// [100] θ-$Al_{13}Fe_4$
C. $(\bar{2}01)$ θ-$Al_{13}Fe_4$ // 2.3° $(0\bar{1}1)$α-Al_{15}(Fe, Mn)$_3Si_2$, and [010] θ-$Al_{13}Fe_4$ // [100] α-Al_{15}(Fe, Mn)$_3Si_2$

(4) The composition of different FIMCs solidified at different conditions are variable, which caused the corresponding lattice parameters change. The Si concentration in different FIMCs has a sequence as: $C_{\theta}^{Si} < C_{\alpha}^{Si} < C_{\alpha'}^{Si} < C_{\beta}^{Si}$.

CRediT authorship contribution statement

Zhongping Que: Conceptualization, Methodology, Investigation, Writing – review & editing. **Changming Fang:** DFT calculation. **Chamini L Mendis:** Partial investigation, reviewing. **Yun Wang:** Partial investigation. **Zhongyun Fan:** Supervision, Visualization, Funding acquisition.

Data Availability

No data was used for the research described in the article.

Declaration of Competing Interest

The authors declare the following financial interests/personal relationships which may be considered as potential competing interests: Zhongyun Fan reports financial support was provided by epsrc. Zhongyun fan reports a relationship with Engineering and Physical Sciences Research Council that includes: funding grants.

Acknowledgement

The Engineering and Physical Sciences Research Council (EPSRC) is gratefully acknowledged for providing financial support under Grant EP/N007638/1. Dr Lorna Auguilano, and Professor Chris Frampton is gratefully acknowledged for supporting in single crystal experiments.

References

[1] L. Zhang, J. Gao, L. Nana, W. Damoah, D.G. Robertson, Removal of Iron from aluminium: A Review, Min. Proc. Ext. Met. Rev. 33 (2012) 99–157.
[2] M.E. Schlesinger, Aluminium recycling, Taylor & Francis group, Milton Park, Abingdon-on-Thames, Oxfordshire 2017.
[3] M. Cooper, The crystal structure of the ternary alloy α(AlFeSi), Acta Cryst. 23 (1967) 1106–1107.
[4] V. Hansen, B.C. Hauback, M. Sundberg, C. Romming, J. Gjonnes, β-$Al_{4.5}FeSi$, a combined synchrotron powder diffraction, electron diffraction, high-resolution electron microscopy and single-crystal X-ray diffraction study of a faulted structure, Acta Cryst. Sect. B Struct. Sci. 54 (1998) 351–357.
[5] C. Gueneau, C. Servant, F. d'Yvoire, N. Rodier, FeAl3Si2, Acta Crystall., Section C: Crystal Structure Communications, 51(1995) 177–179.
[6] J. Grin, U. Burkhardt, M. Ellner, K. Peters, Refinement of the Fe_4Al_{13} structure and its relationship to the quasihomological homeotypical structures, Z. Krist. (1979-2010) 209 (1994) 479–487.

[7] R.N. Corby, P.J. Blabk, The structure of alpha-(Al Fe Si) by anomalous dispersion methods, Acta Crystallographica, Section B: Structural Crystallography and Crystal, Chemistry 33 (11) (1977) 3468–3475.

[8] S. Kumar, P.S. Grant, K.A.Q. O'Reilly, Evolution of Fe bearing intermetallics during DC casting and homogenization of an Al-Mg-Si Al alloy, Metallur. Mater. Trans. A 47 (2016) 3000–3014.

[9] C.M. Dinnis, J.A. Taylor, A.K. Dahle, As-cast morphology of iron-intermetallics in Al-Si foundry alloys, Scr. Mater. 53 (2005) 955–958.

[10] Z.P. Que, Y.P. Zhou, Y. Wang, Z. Fan, Effect of MgO on Phase Selection in Al–Mg–Si–Fe–Mn Alloys, Trans. Indian. Inst. Met. 68 (2015) 1167.

[11] Z.P. Que, Y. Wang, Z. Fan, Formation of the Fe-containing intermetallic compounds during solidification of Al-5Mg-2Si-0.7 Mn-1.1 Fe alloy, Metall. Mater. Trans. A 49 (2018) 2173–2181.

[12] X. Fang, G. Shao, Y.Q. Liu, Z. Fan, Effects of intensive forced melt convection on the mechanical properties of Fe containing Al–Si based alloys, Mater. Sci. Eng. A 445–446 (2007) 65–72.

[13] Hyun You Kim, Tea Young Park, San Won Han, Hyuck Mo Lee, Effects of Mn on the crystal structure of α-Al(Mn,Fe)Si particles in A356 alloys, J. Cryst. Growth 15 (2006) 207–211.

[14] S.G. Shabestari, M. Ghanbari, Effect of plastic deformation and semisolid forming on iron–manganese rich intermetallics in Al–8Si–3Cu–4Fe–2Mn alloy, J. Alloy. Compd. 508 (2010) 315–319.

[15] Y. Cai, R. Liang, L. Hou, J. Zhang, Effect of Cr and Mn on the microstructure of spray-formed Al-25Si-5Fe-3Cu alloy, Mater. Sci. Eng. A 528 (2011) 4248–4254.

[16] G. Gustafsson, T. Thorvaldsson, G. Dunlop, The influence of Fe and Cr on the microstructure of cast Al-Si-Mg alloys, Metall. Trans. A 17 (1986) 45–52.

[17] M. Sha, S. Wu, X. Wang, L. Wan, Effects of Co addition on Fe-bearing intermetallic compounds and mechanical properties of AlSi20Cu2Ni1Fe0.7–1 alloys, J. Alloy. Compd. 551 (2013) 468–474.

[18] A. Lui, P.S. Grant, I.C. Stone, K.A.Q. O'Reilly, The role of grain refiner in the nucleation of AlFeSi intermetallic phases during solidification of a 6xxx aluminum alloy, Metallur. Mater. Trans. A 50 (2019) 5242–5252.

[19] Z.P. Que, Y. Wang, Y.P. Zhou, Y. Wang, Z. Fan, Effect of Al-5Ti-1B grain refiner addition on the formation of intermetallic compounds in Al-Mg-Si-Mn-Fe alloys, Mater. Sci. Forum 828–829 (2015) 53–57.

[20] Z.P. Que, Y.P. Zhou, Y. Wang, Z. Fan, Composition templating for heterogeneous nucleation of intermetallic compounds, Solidif. Process. (2017) 158–161.

[21] Z. Que, C.L. Mendis, Formation of θ-$Al_{13}Fe_4$ and the multi-step phase transformations to α-Al_8Fe_2Si, β-Al_5FeSi and δ-Al_4FeSi_2 in Al-20Si-0.7Fe alloy, Intermetallics 127 (2020) 106960.

[22] Z. Que, C.L. Mendis, Heterogeneous nucleation and phase transformation of Fe-rich intermetallic compounds in Al–Mg–Si alloys, J. Alloy. Compd. 836 (2020) 155515.

[23] Z. Que, Y. Wang, Z. Fan, Heterogeneous nucleation of eutectic structure in Al-Mg-Si alloys, Metall. Mater. Trans. A 51A (2020) 2697–2702.

[24] C.M. Fang, Z. Que, A. Dinsdale, Z. Fan, Si solution in θ-$Al_{13}Fe_4$ from first-principles, Intermetallics 126 (2020) 106939.

[25] J. Roger, F. Bosselet, J.C. Viala, Structural chemistry and thermal stability of the ternary compound alpha - Al Fe Si, J. Solid State Chem. 184 (5) (2011) 1120–1128.

[26] V. Stefaniay, A. Griger, T. Turmezey, Intermetallic phases in the aluminium-side corner of the AlFeSi-alloy system, J. Mater. Sci. 22 (1987) 539–546.

[27] S. Belmares-Perales, M. Castro-Roman, M. Herrera-Trejo, L.E. Ramirez-Vidaurri, Effect of cooling rate and Fe/Mn weight ratio on volume fraction of α-AlFeSi and β-AlFeSi phases in Al-7.3Si-3.5Cu alloy, Metal. Mater. Inter. 41 (3) (2008) 307–314.

[28] P. Popčević, A. Smontara, J. Ivkov, M. Wencka, M. Komelj, P. Jeglič, S. Vrtnik, M. Bobnar, Z. Jagličić, B. Bauer, P. Gille, H. Borrmann, U. Burkhardt, Yu. Grin, J. Dolinšek, Anisotropic physical properties of the $Al_{13}Fe_4$ complex intermetallic and its ternary derivative $Al_{13}(Fe,Ni)_4$, Phys. Rev. B 81 (2010) 184203.

[29] Y. Yang, S.Y. Zhong, Z. Chen, M. Wang, N. Ma, H. Wang, Effect of Cr content and heat-treatment on the high temperature strength of eutectic Al–Si alloys, J. Alloy. Compd. 647 (2015) 63–69.

[30] C. Freiburg, B. Grushko, An Al13Fe4 phase in the AlCuFe alloy system, J. Alloy. Compd. 210 (1–2) (1994) 149–152.

[31] K. Saito, K. Sugiyama, K. Hiraga, $Al_{13}M_4$-type structures and atomic models of their twins, Mater. Sci. Eng. A 294–296 (2000) 279–282.

[32] N.C.W. Kuijpers, F.J. Vermolen, C. Vuik, P.T.G. Koenis, K.E. Nilsen, S. van der Zwaag, The dependence of the β-AlFeSi to α-Al(FeMn)Si transformation kinetics in Al–Mg–Si alloys on the alloying elements, Mater. Sci. Eng. A 394 (2005) 9–19.

[33] H. Becker, T. Bergh, P.E. Vullum, A. Leineweber, Y. Li, β- and δ-Al-Fe-Si intermetallic phase, their intergrowth and polytype formation, J. Alloy. Compd. 780 (2019) 917–929.

[34] Y.S. Choi, J.S. Lee, W.T. Kim, H.Y. Ra, Solidification behavior of Al-Si-Fe alloys and phase transformation of metastable intermetallic compound by heat treatment, J. Mater. Sci. 34 (1999) 2163.

[35] Standard Test Procedure for Aluminium Alloy Grain Refiners: TP-1, Aluminium Association, Washington DC, 1987.

[36] Z.P. Que, Y. Wang, Z. Fan, X.R. Zhou, Q.M. Ramasse, Interfacial segregation of Fe and Si at Al/TiB2 interface, in preparation.

[37] K. Saito, K. Sugiyama, K. Hiraga, $Al_{13}M_4$-type structures and atomic models of their twins, Mater. Sci. Eng. A 294–296 (2000) 279–282.

[38] C. Rømming, V. Hansen, J. Gjønnes, Crystal structure of β-$Al_{4.5}$FeSi, Acta Cryst. B50 (1994) 307–312 (ICSD 74569).

[39] Y.H. Liu, X.Y. Chong, Y.H. Jiang, R. Zhou, J. Feng, Mechnical properties and electronic structures of Fe-Al intermetallic, Phys. B 506 (2017) 1–11.

[40] M.S. Lucas, O. Delaire, et al., Effects of vacancies on phonon entropy of B2 FeAl, Phys. Rev. B 80 (2009) 214303.

[41] C.M. Fang, Z.P. Que, Z. Fan, Crystal chemistry and electronic structure of the β-AlFeSi phase from first-principles, J. Solid State Chem. 299 (2021) 122199.

[42] Y. Wang, C.M. Fang, L. Zhou, T. Hashimoto, X. Zhou, Q.M. Ramasse, Z. Fan, Mechanism for Zr poisoning of Al-Ti-B based grain refiners, Acta Mater. 164 (1) (2019) 428–439.

[43] Y. Wang, Z. Que, T. Hashimoto, X. Zhou, Z. Fan, Mechanism for Si poisoning of Al-Ti-B grain refiners in Al alloys, Metall. Mater. Trans. A 51 (2020) 5743–5757.

[44] C.M. Allen, K.A.Q. O'Reilly, B. Cantor, P.V. Evans, Intermetallic phase selection in 1XXX Al alloys, Prog. Mater. Sci 43 (1998) 89–170.

[45] J. Xia, Z. Que, C.L. Mendis, Z. Fan. Evolution of primary Fe-containing phases in an Al-4Si-4Fe alloy, in preparation.

[46] G. Kresse, J. Hafner, Ab initio molecular-dynamics simulation of the liquid-metal-amorphous-semiconductor transition in germanium, Phys. Rev. B49 (1994) 14251–14269.

[47] J.P. Perdew, K. Burke, M. Ernzerhof, Generalized gradient approximation made simple, Phys. Rev. Lett. 77 (1996) 3865–3868.

[48] https://computherm.com/panaluminum.

[49] Z. Que, Y. Wang, C. Mendis L., C. Fang, J. Xia, X. Zhou, Z. Fan, Understanding Fe-Containing Intermetallic Compounds in Al Alloys: An Overview of Recent Advances from the LiME Research Hub, Metals 12 (10) (2022) 1677.